Effect of photoexcitation on high-harmonic generation in semiconductors

BRIAN DE KEIJZER,[1] PIETER J. VAN ESSEN,[1] AND PETER M. KRAUS[1,2,*]

[1]*Advanced Research Center for Nanolithography, Science Park 106, 1098 XG, Amsterdam, The Netherlands*
[2]*Department of Physics and Astronomy, and LaserLaB, Vrije Universiteit, De Boelelaan 1105, 1081 HV Amsterdam, The Netherlands*
*kraus@arcnl.nl

Solid-state high-harmonic generation is intrinsically sensitive to band structure, carrier population, and carrier scattering. As such, solid-state high-harmonic generation is increasingly used as a probe for femtosecond time-resolved pump-probe experiments. So far, most experimental pump-probe studies have reported photoexcitation-induced amplitude suppression of high-harmonic generation in solid-state media, yet the origins of this phenomenon remain elusive. Through simulations based on the semiconductor Bloch equations, we identify the dephasing of the coherent carrier population as the primary mechanism driving this suppression. Furthermore, we find band gap renormalization to be a source for phase shifts of high harmonics. We introduce an analytical model, based on a semi-classical action, that supports our numerical outcomes.

1. INTRODUCTION

Gas-phase high-harmonic generation (HHG) is the cornerstone of attosecond science [1–4] and is currently maturing towards industrial applications [5–8]. A notable success story among the many applications was HHG from molecules, which helped resolve ionization-induced dynamics [9,10] and was used to probe photoinduced molecular dynamics [11–14]. Notably, the possibility of resolving the amplitude and phase of HHG simultaneously in interferometric measurement techniques enabled linking the observables to changes in the ionization potential (phase) and internuclear separation (amplitude) for simple molecular systems [11,14]. While this provides versatile insight, the molecular gas-phase HHG is restricted to small molecules in the gas phase or to molecules with sufficiently high vapor pressure.

The recent progress on solid HHG has shown that solid HHG is sensitive to the electronic band structure [15,16], and can be generated from many materials [17]. As such, a number of time-resolved studies have already been carried out that have demonstrated that solid HHG is a potent probe of transient, light-induced phenomena. These include measurements of phase transitions via solid HHG [18–20], carrier dynamics in perovskites [21], electron dynamics in semiconductors [22–26], topological surface states, phase transitions, and unusually long scattering times in topological insulators [27,28], to name a few. Common to most of these experiments was a near-universal observation of a reduced HHG emission intensity following photoexcitation [29]. This provides a powerful opportunity

to control light emission on the nanoscale [30–32], and was recently demonstrated to be a possible tool for super-resolution microscopy [33].

Both understanding the sensitivities of HHG to light-induced dynamics to enable HHG spectroscopy and improving emission control concepts require understanding the microscopic origins of HHG signal changes following photoexcitation. Early papers speculated that ground-state depletion due to photoexcitation may play a role [22,23,34]. More recent work mentioned that also small amounts of carrier excitation might cause changes to the electron-hole dephasing time via increased carrier scattering [25,35,36]. Here we shed light on this important question by numerical simulations of HHG from photoexcited solids. We use semiconductor Bloch equations to identify that ground-state depletion, or an excited incoherent carrier population, has a minor effect on HHG. However, changes in dephasing time and band gap shrinkage have major effects on HHG amplitude and phase, respectively. We verify these findings with an analytical two-band model. In the current manuscript, we focus on pump-induced phenomena outside pump-probe overlap, as HHG during overlapping multicolor pulses is better described as HHG from shaped waveforms similar to the work on gas HHG [37–39].

The paper is organized as follows: in Section 2, we describe the general microscopic theory behind the semiconductor Bloch equations that are used to numerically simulate HHG. In Section 3, we give more details of our specific model. In Section 4, we present the results of our numerical model.
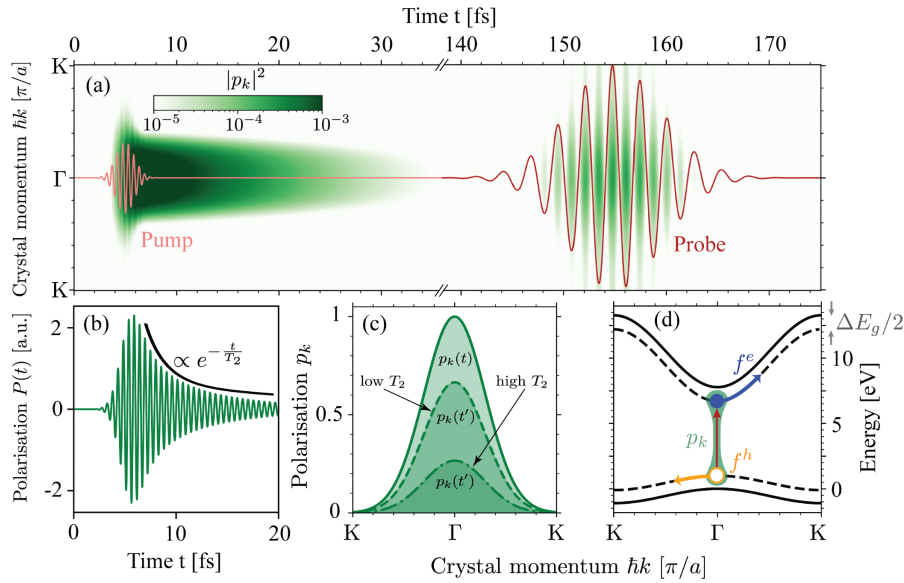
Fig. 1. Sketches of the various simulations performed in this work. (a) Electric field of pump and probe pulses (red) and the resulting microscopic polarization (green) in the conduction band. An eight-cycle pump of 158 nm with peak intensity 10^{11} W/cm^2 is applied. This is followed by an eight-cycle 800 nm probe with peak intensity 10^{12} W/cm^2. (b) Macroscopic polarization resulting from the pump. The exponential is to guide the eye. (c) A schematic of varying dephasing time T_2 and its effect on the microscopic polarization at different times t and t'. (d) The microscopic objects under consideration. Photoexcitation (red) yields electron-hole pairs (blue and yellow) that may be coherent (green). This results in intra- (blue and yellow) and interband contributions (green) to the spectrum. The dashed line depicts the approximated conduction band after band gap renormalization.

In Section 5, we discuss these results aided by an analytical model based on a two-band approximation, classical coherent electron-hole trajectories, and localized excitation in k-space. In Section 6, we provide a conclusion and outlook.

2. MICROSCOPIC THEORY OF SOLID-STATE HIGH-HARMONIC GENERATION

A collinear pump-probe experimental configuration is simulated along a single-crystal direction of a two-band model using the semiconductor Bloch equations. The results are shown in Figs. 1(a)–1(c) and discussed in depth in the next section. The numerical problem is constructed to mimic cubic MgO along the $\Gamma - K$ direction where we assume tight binding sinusoidal bands shown in Fig. 1(d). We use a band gap of $E_g = 7.8$ eV [40], a valence band height of 0.5 eV, a conduction band height of 2.92 eV, and a lattice constant $a = 4.19$ Å. The transition dipole moment is approximated using first order $\mathbf{k} \cdot \mathbf{p}$ theory [41,42]:

$$d_k = d_0 \frac{E_g}{\epsilon_k^e - \epsilon_k^h}, \qquad (1)$$

with $d_0 = 0.372$, a.u. being the transition dipole moment at the Γ-point and $\epsilon_k^{e(h)}$ the single-particle energies of the conduction (valance) band. The dipole moment at the Γ-point is obtained based on Quantum Espresso calculations with generalized gradient approximation in the shape of the Perdew and Zunger functionals. While the dipole moments depend more on the exact choice of the simulation parameters than, e.g., the bands, we checked that the exact value of d_0 does not influence our observations. We drive the system using Gaussian envelope

$E(t) := E_0 \cos(\omega_0 t) \exp(-(2\sqrt{\ln(2)}\frac{t}{\tau})^2)$ pulses with peak electric field E_0, frequency of the field ω_0, and pulse duration τ. We then numerically solve the semiconductor Bloch equations without carrier recombination and without Coulomb interaction:

$$i\hbar \frac{\partial}{\partial t} p_k = \left(\epsilon_k^e + \epsilon_k^h - i\frac{\hbar}{T_2} \right) p_k - (1 - f_k^e - f_k^h)d_k E(t)$$
$$+ i e E(t) \cdot \nabla_k p_k, \qquad (2)$$

$$\hbar \frac{\partial}{\partial t} f_k^{e(h)} = -2 \operatorname{Im}[d_k E(t) p_k^*] + e E(t) \cdot \nabla_k f_k^{e(h)}, \qquad (3)$$

using sparse spectral methods [43] on a one-dimensional complex Fourier basis in order to obtain the microscopic polarization p_k and microscopic population $f_k^{e(h)}$. Convergence is achieved using 129 points in k-space with a propagation time-step of 10 attoseconds, resulting in a simulation time of <5 min using a single Apple M1 core.

To obtain the high-harmonic emission spectrum we calculate the macroscopic *interband* polarization

$$P(t) = \sum_k [d_k p_k(t) + \text{c.c.}] \qquad (4)$$

and the macroscopic *intraband* current

$$J(t) = \sum_{\lambda,k} e v_k^\lambda f_k^\lambda(t), \qquad (5)$$

with $\lambda \in \{e, h\}$ and group velocity

$$v_g^\lambda = \frac{1}{\hbar}\frac{\mathrm{d}}{\mathrm{d}k}\epsilon_k^\lambda. \tag{6}$$

The near-field emission spectrum is then obtained by summing the contributions from interband polarization and intraband current [44]:

$$I_{\mathrm{rad}}(\omega) \propto |\omega^2 P(\omega) + i\omega J(\omega)|^2. \tag{7}$$

The details of our model were also explained in previous publications [45,46].

To minimize spectral leakage from the pump pulse, we apply a Hanning window to the macroscopic polarization and macroscopic current in the time domain around the time window of the probe pulse that generates harmonics before computing the spectra. In order to analyze the phase and amplitude modulation of harmonic order HO, we apply another Hanning window in the spectral domain to the complex-valued spectrum, centered symmetrically around the harmonic order of interest HO ± 0.25 all throughout this work. The result is then inverse Fourier transformed in order to obtain the emitted electric field for a selected frequency. Within the phase analysis, we typically consider only $P(\omega)$. This is because $P(\omega)$ is usually dominant for above band gap harmonics [17], which we independently numerically verified in all simulations shown in the present manuscript.

3. SIMULATION FRAMEWORK

In order to analyze the effect of photoexcitation on high-harmonic generation we simulate a typical pump-probe experiment. The pulse parameters are chosen to be representative of an experimental setting; the low-intensity pump is one-photon resonant with the band gap whereas the harmonic generation probe pulse has a longer wavelength far below the band gap with an intensity chosen such that it is slightly below the experimentally found damage threshold of the material. Initially, we consider the pulse sequences in Fig. 1(a) where the system is either pumped or not prior to the probe. The effects on carrier scattering in this scenario are illustrated in Figs. 1(b) and 1(c), and the corresponding processes are depicted in Fig. 1(d). This approach allows to isolate the effects of photoexcitation by the pump. Doing so justifies not pumping the system in further simulations. Consecutively we consider two particular many-body effects under typical carrier densities $\chi \in [10^{18}, 10^{20}]$ cm^{-3} and lastly combine their effects.

Firstly we consider the effect of increasing carrier density on the scattering of the coherent population. This increase results in increasing dephasing time T_2 of the coherent population. T_2 is a phenomenological addition to the SBE that encapsulates all many-body interactions effecting the coherent population; this includes carrier-carrier scattering and carrier-phonon scattering [47–49]. The effect of dephasing is sketched in Figs. 1(b) and 1(c). Using the experimental findings and phenomenological model of Ref. [50] we determine a typical range for this dephasing time, which is presented in Fig. 2. This independently reproduces the observed relative T_2 scaling in Ref. [25], where a similar method is used to obtain the dephasing time, albeit in a transition metal dichalcogenide sample. This highlights the
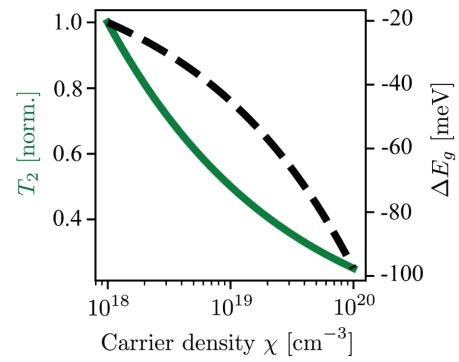
Fig. 2. Effect of carrier density on the dephasing time $T_2 \propto \chi^{-0.3}$ normalized to $T_2 = 19$ fs (left vertical axis, proportionality taken from Ref. [50]) and band gap renormalization (right axis).

agreement on the scaling of T_2. However, noting the phenomenological nature of T_2, no direct experimental comparison is to be made. It should be noted that several nonlinear experimental spectroscopy techniques ranging from photon echo to four wave mixing [50–52] as well as photocurrent generation [53] and femtosecond two-photon photoemission [54] exist to extract dephasing times, often for single-photon excitation close to the Γ point. While those give a good indication, these dephasing times are not necessarily the same as those relevant to solid HHG, which are driven by multiphoton excitations as well as intraband electron-hole accelerations to high carrier momenta.

We then perform independent simulations per value of T_2 to consider its effect on high-harmonic generation.

Second, Ref. [55] reported a widely used phenomenological model that described experimental data for band gap shrinkage with increasing carrier density χ: $\Delta E_g(\chi) = \frac{\kappa}{\epsilon_s}(1 - \frac{\chi}{\chi_{\mathrm{cr}}})^{1/3}$, where κ is a fitting parameter, χ_{cr} is the critical concentration of free carriers, and ϵ_s is the relative static dielectric constant of the semiconductor. We use this model to estimate typical ΔE_g values as seen in Fig. 2. To model the renormalization effect we then perform independent simulations per value of ΔE_g as depicted in Fig. 1(d). We thus approximate the band gap renormalization as linear all across k.

Lastly, both effects are combined providing a simple but effective microscopic picture of the effect of photoexcitation on high-harmonic generation.

4. NUMERICAL RESULTS

We start by simulating the pump-probe experimented schematically depicted in Fig. 1(a). To allow for the accumulation of coherent population within the (pump) probe simulation(s) we choose a dephasing time larger than one optical cycle, thus defining $T_2 = 10$ fs. We define the delay between the envelope peaks of the pulses to be 150 fs $\gg T_2$ such that all pump-induced microscopic polarization, that is, coherence, prevails prior to the probe. Within this work, we denote different simulations using dashed and solid lines. The total spectral contributions are shown in shades of orange, whereas the interband and intraband contributions are shown in green and blue, respectively.

As in Ref. [56], we observe from Fig. 3(a) the pump to enhance below band gap generation, which we elaborate below.
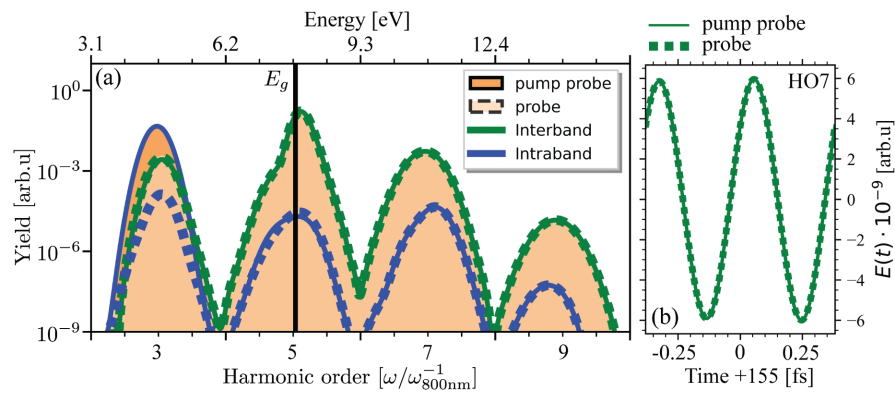
Fig. 3. (a) Spectral contributions from the pump-probe (solid lines) and probe (dashed lines) simulations. The total contributions are shown with an infill whereas interband and intraband are shown in green and blue, respectively. (b) Reconstructed electric fields for the seventh harmonic (HO7) under double- and single-pulse scenarios.
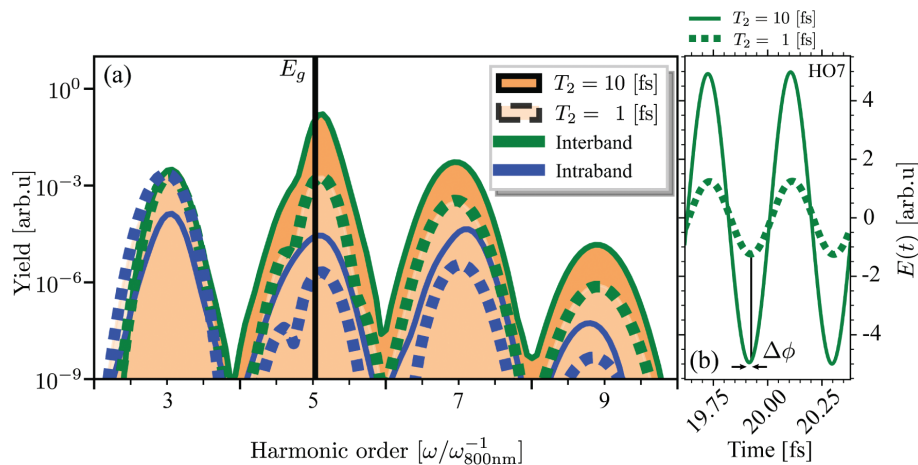
Fig. 4. Effect of dephasing time on high-harmonic generation. A reduction of dephasing time is expected after photoexcitation to last for as long as there are incoherently excited carriers. (a) Resulting contributions to the spectrum for longer and shorter dephasing times. (b) Reconstructed electric fields of the seventh harmonic (HO7) for various dephasing times. The vertical black line is to guide the eye.

The intraband contribution is substantially enhanced below the band gap - that is, below the energy initially provided by the single-photon excitation - when the system is pumped prior to the probe. This occurs as the single-photon excitation provides additional carriers that contribute to the low-energy, below-band gap part of the intraband current. We thus see that photoexcitation may enhance below-band gap intraband dominated harmonics from a *microscopic* point of view. However, this picture may be called into question when also considering *macroscopic* effects, i.e., phase matching, as emission from the incoherently excited carriers may not provide a fixed phase relationship that is needed for the coherent buildup of HHG.

We now analyze the phase of HHG following photoexcitation in the present simulation configuration. Figure 3(b) shows the emitted electric field over two cycles of harmonic seven, obtained by filtering harmonic seven of the complex-valued spectrum and Fourier transforming back into the spectral domain as described above. Here we observe no amplitude nor phase change when comparing (pump-) probe sequences. This result is consistent among all observed above-band gap harmonics. Thus, to simplify the model and ease computation,

the pump pulse is left out in further simulations where we focus on the above-band gap harmonics.

Notably, we consistently observe spectral asymmetry of the harmonic around the band gap for varying band gaps. Thus we relate the dip in the left shoulder of the fifth harmonic in Fig. 3(a) to the band gap, specifically to band gap emission that is always present in the simulations.

To analyze the effects of reduced dephasing time, which is known to be an accompanying multielectron effect of photoexcitation, Fig. 4(a) illustrates the spectral change caused by different values in dephasing time with respect to the optical cycle length of the probe. Note that a decrease in dephasing time is due to increased carrier scattering. That means that we expect a reduction of dephasing time right after photoexcitation, and to last as long as there is (incoherent) carrier population, which typically is on the order of picoseconds to nanoseconds. In Fig. 4(b) the total yield for all harmonics significantly drops for low dephasing times as supported by recent findings [25,56–59]. This is quantified in Fig. 4(b), where we again analyze the time-profile of harmonic seven. Here we observe a significant yield decrease for dephasing times smaller than two optical cycles. We relate this to increased scattering resulting in less
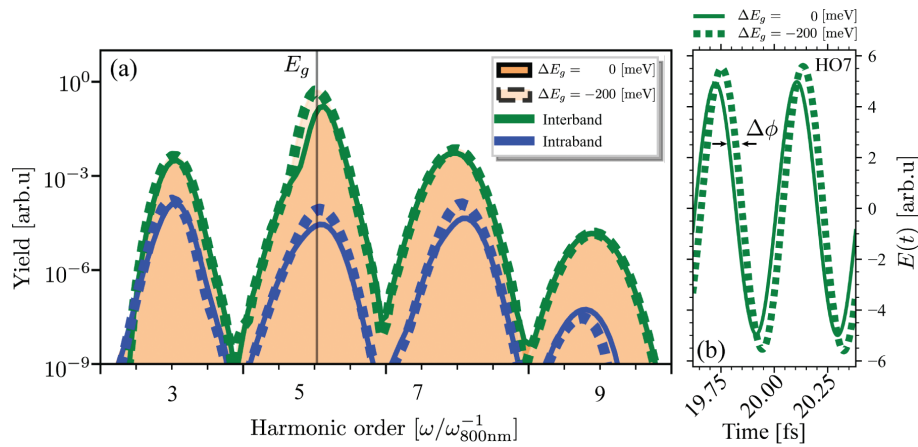
Fig. 5. Effect of band gap renormalization under a single-pulse scenario without a probe. (a) Resulting contributions to the spectrum for smaller and larger band gap renormalization. (b) Reconstructed electric fields for the seventh high harmonic (HO7) with and without band gap renormalization.
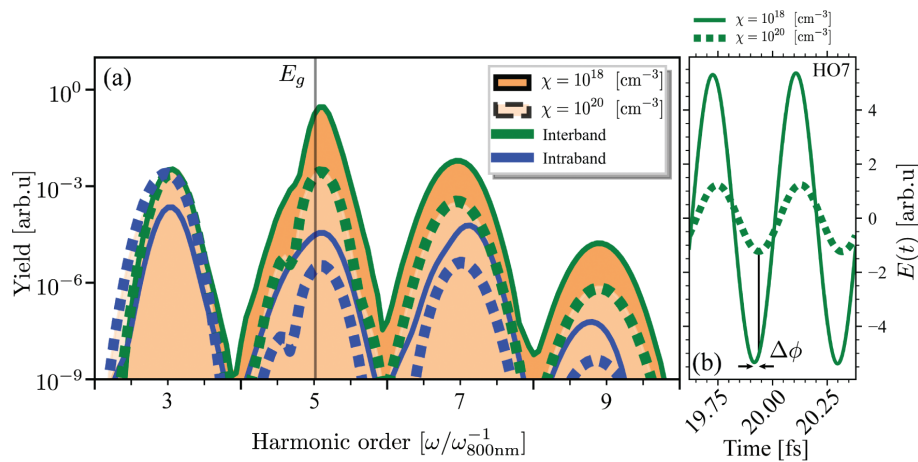
Fig. 6. Combined effect of band gap renormalization and varying scattering of the coherent population as a function of carrier density under a single-pulse scenario. (a) Resulting contributions to the spectrum for smaller and larger carrier densities. (b) The effect of carrier density on the phase of harmonics. The vertical black line serves as a guide to the eye.

microscopic polarization to be accumulated over the duration of the laser pulse, resulting in a yield decrease. Additionally, a phase change is observed. We attribute this phase change to the gradual change in the dominant (sub-)optical cycle in which most of the harmonic is emitted. This is explained by the time-dependent change in the accumulated coherent population along the duration of the laser pulse.

Furthermore we analyze the effects of band gap shrinkage on high-harmonic generation, another multielectron effect known to occur following photoexcitation [55]. The nuances of band gap renormalization and its effect on the spectrum, particularly around the band gap, are captured in Fig. 5. In particular, we display band gap renormalization for selected values in Figs. 5(a) and 5(b). Inverse Fourier transforming harmonic seven uncovers band gap renormalization to cause a significant phase change $\Delta\phi$. Figure 5(b) quantifies the phase change for large ΔE_g. Here we observe that harmonics with energies $\geq E_g$ undergo significant phase change.

Combining the two many-body effects reveals varying carrier density to cause both amplitude and phase modulation as

observed in Fig. 6. We observe a reduction of overall emission, that is, amplitude, both visible in the spectrum in Fig. 6(a) and the time-domain signal of harmonic seven in Fig. 6(b). We also see a clear phase shift of the emitted harmonics. This is illustrated for the seventh harmonic in Fig. 6(b), where a 0.14 rad absolute phase shift is observed. As elaborated above, the amplitude reduction is due to increased carrier scattering, which is synonymous with a reduction of the dephasing time, and the phase shift is due to band gap shrinkage. These results establish the qualitative phase shifts and amplitude suppression following the multielectron effects induced by photoexcitation. In the next section, we present quantitative pump intensity scalings and compare to an analytical theory.

5. DISCUSSION AND SUPPORTING ANALYTICAL MODEL

To support the numerical simulations we develop an analytical model that evaluates the semi-classical laser-driven carrier trajectories and incorporates the multielectron effects of band
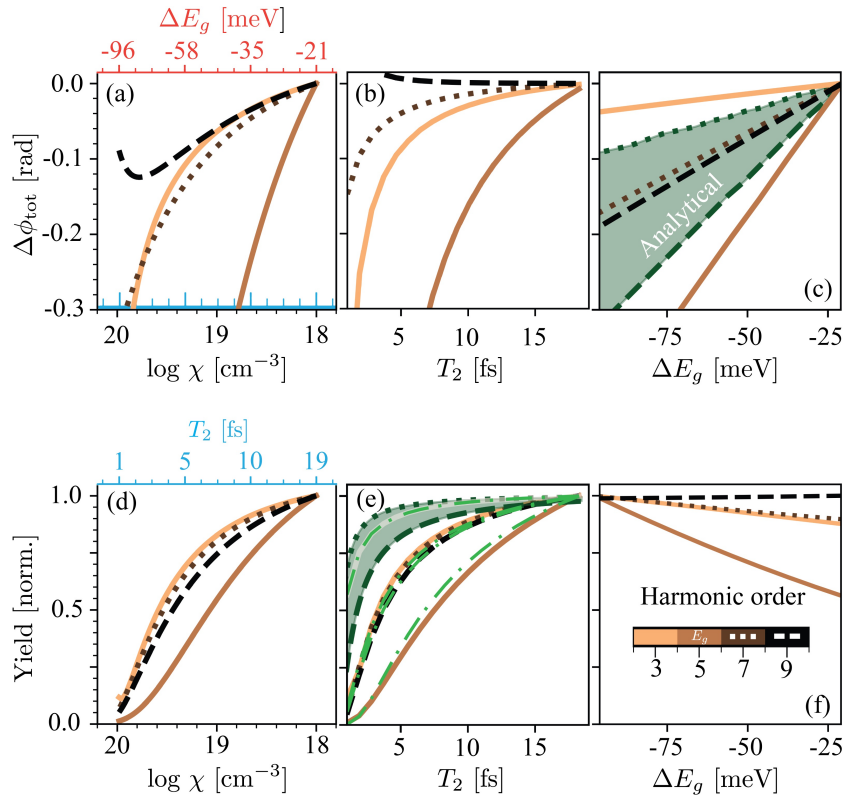
Fig. 7. Solid-state HHG (a)–(c) phase and (d), (f) amplitude changes. Numerical results as function of (a), (d) combined band gap renormalization and varying dephasing time; (b), (e) dephasing time; (c), (f) band gap renormalization. Shades of brown indicate numerical results of Figs. 2–6 based on the semiconductor Bloch equations. Filled shades of dark green indicate the analytical theory, Eq. (13), of HO7 for both long trajectories (dashed) and short trajectories (dotted). The analytical theory uses a peak intensity of 7 TW/cm² and encompasses HO7 and HO9 in panel (c). The light green dashed-dotted lines in (e) indicate analytical theory, Eq. (17), based on fitted characteristic excursion times from (c).

gap renormalization and carrier scattering with the same phenomenological expressions introduced in the previous sections. The analytical results are depicted in Fig. 7 together with the extended results from the previous section. Figure 7 shows phase (a)–(c) and amplitude (d)–(f) changes caused by simultaneous band gap renormalization and dephasing-time reduction (a), (d); dephasing-time reduction (b), (e); and band gap renormalization (c), (f). The semiconductor Bloch equation (SBE) results in Fig. 7 are shown in shades of orange/brown, and the results from the analytical model introduced in this section are shown in green. In the following, we discuss the results from the previous section and introduce the analytical model concurrently, aiming for a thorough understanding of the observed phenomena in each panel of Fig. 7.

The combined effect of both many-body effects on the phase and amplitude as a function of carrier density is shown in Figs. 7(a) and 7(d). Note the scaling is in the base 10 logarithm of carrier density and thus non-linear in both T_2 (blue) and ΔE_g (red). Both panels nicely display results consistent with the underlying effects as discussed before. An exception here is the phase of harmonic nine, which increases for very short dephasing times. We attribute the increasing phase change of harmonic nine at sub-optical cycle dephasing times to the uncertainty in yield as it reaches the numerical noise floor.

In Fig. 7(b) we observe a strong phase change for harmonic five, which is located at the band gap. This is explained by a

decreasing band gap; this allows for increasing accumulation of population, manifesting itself in increasing emission earlier during the pulse envelope. This furthermore quantifies the phase change as observed earlier in Fig. 4(b). We relate the phase change by varying T_2 to a truncation of the time over which harmonics are rejected, which may be interpreted classically as the transit times of the electron trajectories. This can further cause a gradual change in the dominant emitting optical cycle. This is explained by longer T_2 allowing for more accumulated population to exist posterior to the pulse envelope peak. In return decreasing T_2 shifts the apparent maximum in population (emission) to an earlier moment in time. Consecutively the phase change caused by T_2 becomes significant as T_2 reaches (sub-)optical cycle timescales.

To provide more insight into the numerical findings, we establish an analytical model. For this, classical trajectories are obtained by considering the SBEs for two bands in the limit of low carrier inversion. The semi-classical description can be derived from the SBEs by using the interband saddle point approximation [60]. For the analytical model, we use identical band structure and a transition dipole moment as the numerical simulations. The trajectories are solved for a single optical cycle of the driving field. The effective carrier momentum for a specific excitation time t_i is determined by the external field as

$$k(t) = A(t) - A(t_i) + k_0. \tag{8}$$

Here $A(t)$ denotes the vector potential. We assume a perfect cosine driving field allowing us to express the vector potential as

$$A(t) = -\int E(t)\mathrm{d}t = -\frac{E_0}{\omega_0} \sin(\omega_0 t). \qquad (9)$$

Only excitation from the Γ-point is considered, so $k_0 = 0$. By limiting the excitation to a single point in k-space we obtain distinct long and short trajectories. The SBE simulation does not yield distinct trajectories as excitation all along the bands is allowed [61]. If we try to interpret this from a classical point of view we can consider the SBE simulation resulting in the weighted sum of all possible trajectories. From this we do not expect the SBE simulations to match either with the long or short trajectory results; instead, we expect the long and short trajectories to provide an upper and lower bound enclosing the SBE results.

The trajectories for the different excitation times are obtained classically by integration of the group velocity over time:

$$x^\lambda(t) = \int_{t_i}^{t} v_g^\lambda(k(\tau))\mathrm{d}\tau. \qquad (10)$$

Recombination is assumed to occur when the spatial displacement between the electron and hole goes to zero:

$$\Delta x(t_f) = x^e(t_f) - x^h(t_f) = 0. \qquad (11)$$

Here t_f denotes the recombination time of the trajectory. Only trajectories that recombine contribute to the interband current. The emitted photon energy for a given trajectory is the energy difference between the charge carriers at the time of recombination. The semi-classical model can only evaluate trajectories for the above-band gap and below-cut-off harmonics.

We consider the effects of band gap renormalization on the phase of the interband current. The phase of the emitted light is evaluated via the semi-classical action

$$S(t_f) = \int_{t_i}^{t_f} \Delta\epsilon(k(\tau))\mathrm{d}\tau. \qquad (12)$$

From the semi-classical action, the dipole phase is evaluated [62]:

$$\phi = N_h \left(\omega_0 t_f + \frac{\pi}{2}\right) - S(t_f). \qquad (13)$$

Here N_h is the harmonic order. The dipole phase for HO7 obtained with the analytical model is shown in Fig. 7(c). The long (dark green dashed) and short (dark green dotted) trajectory results for HO7 are shown separately and enclose the numerical results. As predicted, The SBE simulation results show neither behavior that corresponds solely to the short or long trajectories. Both the numerical and analytical models show the phase linearly varying with the band gap shrinkage. For small changes to the band gap, the trajectories and their excitation and recombination times will only vary slightly. Under the condition that the band gap changes are small, we can obtain an approximation of the change in the dipole phase:

$$\Delta\phi \approx \Delta E_g \Delta t, \quad \text{with} \quad \Delta t = t_f - t_i. \qquad (14)$$

This linear relation matches the numerical results and indicates that the phase change is dependent on the Δt of the different harmonic orders. As there are no classical trajectories in the SBE model, Δt can be interpreted as the characteristic excursion time of the harmonic instead of the trajectory duration. We obtain the characteristic excursion times of the harmonics via the use of linear fits on the curves in Fig. 7: $\Delta t_{\text{HO3}} = 0.30\,\text{fs}$, $\Delta t_{\text{HO5}} = 3.85\,\text{fs}$, $\Delta t_{\text{HO7}} = 1.45\,\text{fs}$, and $\Delta t_{\text{HO9}} = 1.63\,\text{fs}$. Except for HO5, we note that the phase change increases with harmonic order. This dependence can be understood as with an increased excursion time, the driving field can accelerate charge carriers to higher energies. The deviating behavior of HO5 can be attributed to this harmonic being close to resonance with the band gap. More specifically, for HO5 the temporal overlap with the band gap emission, which is limited by the much longer T_2, prolongs the characteristic excursion time Δt_{HO5}.

The effect on the harmonic yield as a function of carrier density is displayed in Fig. 7(d). We observe HO5 deviates from the other harmonics and attribute this to the band gap. Notice furthermore that HO3 slightly increases again, around $\chi = 10^{20}\,\text{cm}^{-3}$; we attribute this to numerics and do not conclude it as a physical change.

We now analytically consider the effect of dephasing on the interband current. The interband current can be expressed as [60]

$$j(\omega)$$

$$= \omega \int_{-\infty}^{\infty} \int_{\text{BZ}} \int_{-\infty}^{t} e^{-i\omega t}[d^*(k) \cdot E(\tau) \cdot d(k + A(\tau) - A(t))$$

$$\cdot e^{iS(k,\tau,t)-(t-\tau)/T_2} + \text{c.c.}]\mathrm{d}\tau\,\mathrm{d}^3 k\,\mathrm{d}t. \qquad (15)$$

Here BZ refers to the Brillouin zone. Using the saddle-point approximation we derive an expression for the interband current for a particular trajectory n with excitation time $t_{i,n}$:

$$j_n = C_n \int_{t_{i,n}}^{t_f} \left[d(k_0 + A(\tau) - A(t_{i,n})) \cdot E(\tau) \cdot e^{-(t_f-\tau)/T_2}\right]\mathrm{d}\tau. \qquad (16)$$

Here C_n is a trajectory-dependent constant. The intensity for a given trajectory is obtained by considering the absolute squared value of the current:

$$I_n \propto |j_n|^2. \qquad (17)$$

The intensity for HO7 obtained with the analytical model is shown in Fig. 7(e) using a dark green infill with short trajectories (dotted) and long trajectories (dashed). Although there is a rough qualitative agreement between the analytical and numerical results we note that the numerical results fall entirely outside the analytical range. It is clear that in the numerical simulation, the suppression greatly exceeds that of the analytical model. We attribute this discrepancy to the complete disregard of excitation in our analytical model. While in the SBE simulation the population transfer during excitation is lowered by a smaller T_2 that results in a faster-decreasing polarization, no such mechanism is taken into account in our analytical model. As such the analytical model is missing an additional damping term.

To correct for the change in excitation we consider the effects of T_2 on the population. While T_2 is affecting coherence rather than population in the first instance, a persisting coherence (polarization) has influence on additional population transfer during light-matter interaction. In the limit that the carrier excitation fraction is low, we can approximate the change in population as being proportional to the polarization. In turn, assuming the majority of the polarization is created near the extremes of the electric field we can approximate the polarization between these extremes as an exponential decay:

$$\frac{\partial}{\partial t} f_k^\lambda \approx -2 \operatorname{Im}[d_k E(t) p_k^*] \approx -2 \operatorname{Im}\left[d_k E(t) p_0 e^{-\frac{t}{T_2}}\right]. \tag{18}$$

Here p_0 is a complex constant. Considering this approximation allows us to introduce a correction for the effects of excitation by scaling the current with a factor $\exp(-\Delta t / T_2)$.

We introduce an additional approximation to the current by assuming the dipole coupling to be constant, which allows for direct integration of the integral in Eq. (16):

$$j_n = C_n' \frac{T_2}{1 + T_2^2 \omega_0^2} \left[\cos(\omega_0 t_f) + T_2 \omega_0 \sin(\omega_0 t_f) \right. $$
$$\left. - e^{-\frac{\Delta t}{T_2}} [\cos(\omega_0 t_i) + T_2 \omega_0 \sin(\omega_0 t_i)] \right]. \tag{19}$$

Additionally we simplify our current expression by assuming the excitation and recombination to occur near the peaks of our electric field, $\sin(\omega t_f) = \sin(\omega t_i) = 0$ and $\cos(\omega t_f) = \cos(\omega t_i) = 1$, and by assuming that the dephasing is fast relative to the driving frequency. With these additional assumptions and including the additional term for excitation correction, we obtain

$$I \underset{\sim}{\propto} e^{-\frac{\Delta t}{T_2}} \left| T_2 \left(1 - e^{-\frac{\Delta t}{T_2}}\right) \right|^2. \tag{20}$$

This expression shows that an increased dephasing due to photoexcitation will result in suppression of the HHG intensity. This equation also shows that for longer excursion times suppression will increase, which is expected to correspond to the higher-order harmonics. Interestingly the relation obtained is again characterized solely by the effective excursion time Δt. To evaluate the consistency of this expression, we used the excursion times obtained from the linear fits of the SBE phases shown in Fig. 7(c). These phases were used to plot the intensity as described with Eq. (20); the resulting intensity curves can be seen in Fig. 7(e) (light green dashed-dotted lines). We observe good agreement between the analytical curves and the SBE simulation results for H05, HO7, and HO9, especially considering the significant number of approximations made in the derivation of the analytical expression. For HO3, however, the analytical and SBE results do not match; this makes sense as this harmonic is intraband-dominated and we only consider the interband current in the analytical model.

We also observe minor amplitude changes for increasingly reduced band gaps in our SBE simulations, Fig. 7(f), which is attributed to enhanced strong-field excitation (tunneling) due to a lower band gap, as also expressed in Eq. (1). For HO5 a noticeably stronger amplitude increase is observed as the band gap reduction brings the band gap closer to resonance with the harmonic.

We demonstrated that the numerical SBE simulation results of the phase change due to the band gap shrinkage and the interband intensity change due to dephasing are consistent with the analytical model. Here we found that both these effects in this two-band model can be characterized by an effective excursion time Δt of the different harmonics.

6. CONCLUSION AND OUTLOOK

Within a two-band numerical and analytical model of MgO, we have demonstrated that the multielectron effects initiated by photoexcitation can cause significant signal changes in solid-state high-harmonic generation. Using phenomenological expressions derived in literature from experimental results, we have constructed an approximation to the combined many-body effect of band gap renormalization and varying dephasing time of the coherent population as a function of carrier density. We then isolated these effects and identified that the dephasing time of the coherent population acts like a harmonic-order dependent amplitude suppression of the HHG spectrum and additionally yields harmonic-order dependent non-linear phase shift to the emitted harmonic. We furthermore observe band gap renormalization to yield a linear harmonic-order dependent phase shift to the emitted harmonic. Both effects are induced by carrier excitation and scale with increasing carrier densities. Combining these effects yields both amplitude and phase modulation as a function of carrier density. Additionally, we have shown that we can neglect modifications of the HHG spectrum due to state blocking from the incoherent carrier population excited by a pump pulse for above-band gap harmonics.

Our results provide guidance for interpreting transient high-harmonic spectroscopy of solids and give hints on how prepulse sequences can be designed to optimize the emission control of solid HHG.

To further advance the simulations of HHG from photoexcited solids ab initio multielectron treatments of k-space and carrier-density dependent electron scattering are necessary, ideally integrated into the time-domain integration of the SBEs, but if not, at least in a static picture to gain more predictive insight into the effects of photoexcitation on solid-state HHG.

REFERENCES

1. F. Krausz and M. Ivanov, "Attosecond physics," Rev. Mod. Phys. **81**, 163–234 (2009).

2. P. M. Kraus, M. Zürch, S. K. Cushing, *et al.*, "The ultrafast x-ray spectroscopic revolution in chemical dynamics," Nat. Rev. Chem. **2**, 82 (2018).

3. P. B. Corkum and F. Krausz, "Attosecond science," Nat. Phys. **3**, 381–387 (2007).

4. M. Hentschel, R. Kienberger, C. Spielmann, *et al.*, "Attosecond metrology," Nature **414**, 509–513 (2001).

5. C. Porter, T. Coenen, N. Geypen, *et al.*, "Soft x-ray: novel metrology for 3d profilometry and device pitch overlay," Proc. SPIE **12496**, 412–420 (2023).

6. A. J. den Boef, "Optical wafer metrology sensors for process-robust CD and overlay control in semiconductor device manufacturing," Surf. Topogr. Metrol. Prop. **4**, 023001 (2016).

7. H. Kinoshita, T. Harada, Y. Nagata, *et al.*, "Development of EUV mask inspection system using high-order harmonic generation with a femtosecond laser," Jpn. J. Appl. Phys. **53**, 086701 (2014).

8. A. J. d. Boef, "Optical metrology of semiconductor wafers in lithography," Proc. SPIE **8769**, 57–65 (2013).

9. O. Smirnova, Y. Mairesse, S. Patchkovskii, *et al.*, "High harmonic interferometry of multi-electron dynamics in molecules," Nature **460**, 972–977 (2009).

10. P. M. Kraus, B. Mignolet, D. Baykusheva, *et al.*, "Measurement and laser control of attosecond charge migration in ionized iodoacetylene," Science **350**, 790–795 (2015).

11. H. J. Wörner, J. B. Bertrand, D. V. Kartashov, *et al.*, "Following a chemical reaction using high-harmonic interferometry," Nature **466**, 604–607 (2010).

12. H. J. Wörner, J. B. Bertrand, B. Fabre, *et al.*, "Conical intersection dynamics in No_2 probed by homodyne high-harmonic spectroscopy," Science **334**, 208–212 (2011).

13. P. M. Kraus, Y. Arasaki, J. B. Bertrand, *et al.*, "Time-resolved high-harmonic spectroscopy of nonadiabatic dynamics in NO_2," Phys. Rev. A **85**, 043409 (2012).

14. P. M. Kraus and H. J. Wörner, "Time-resolved high-harmonic spectroscopy of valence electron dynamics," Chem. Phys. **414**, 32–44 (2013).

15. M. Borsch, C. P. Schmid, L. Weigl, *et al.*, "Super-resolution lightwave tomography of electronic bands in quantum materials," Science **370**, 1204–1207 (2020).

16. J. Costello, S. O'Hara, Q. Wu, *et al.*, "Reconstruction of Bloch wavefunctions of holes in a semiconductor," Nature **599**, 57–61 (2021).

17. S. Ghimire and D. A. Reis, "High-harmonic generation from solids," Nat. Phys. **15**, 10–16 (2019).

18. M. R. Bionta, E. Haddad, A. Leblanc, *et al.*, "Tracking ultrafast solid-state dynamics using high harmonic spectroscopy," Phys. Rev. Res. **3**, 023250 (2021).

19. Z. Nie, L. Guery, E. Molinero, *et al.*, "Following the nonthermal phase transition in niobium dioxide by time-resolved harmonic spectroscopy," Phys. Rev. Lett. **131**, 243201 (2023).

20. C. Heide, Y. Kobayashi, D. R. Baykusheva, *et al.*, "Probing topological phase transitions using high-harmonic generation," Nat. Photonics **16**, 620–624 (2022).

21. M. L. van der Geest, J. J. de Boer, K. Murzyn, *et al.*, "Transient high-harmonic spectroscopy in an inorganic–organic lead halide perovskite," J. Phys. Chem. Lett. **14**, 10810–10818 (2023).

22. Z. Wang, H. Park, Y. H. Lai, *et al.*, "The roles of photo-carrier doping and driving wavelength in high harmonic generation from a semiconductor," Nat. Commun. **8**, 1–7 (2017).

23. Y. Wang, F. Iyikanat, X. Bai, *et al.*, "Optical control of high-harmonic generation at the atomic thickness," Nano Lett. **22**, 8455–8462 (2022).

24. Y. Wang, Y. Liu, P. Jiang, *et al.*, "Optical switch of electron-hole and electron-electron collisions in semiconductors," Phys. Rev. B **107**, L161301 (2023).

25. C. Heide, Y. Kobayashi, A. C. Johnson, *et al.*, "Probing electron-hole coherence in strongly driven 2d materials using high-harmonic generation," Optica **9**, 512–516 (2022).

26. M. Schultze, K. Ramasesha, C. Pemmaraju, *et al.*, "Attosecond band-gap dynamics in silicon," Science **346**, 1348–1352 (2014).

27. Y. Bai, F. Fei, S. Wang, *et al.*, "High-harmonic generation from topological surface states," Nat. Phys. **17**, 311–315 (2021).

28. C. P. Schmid, L. Weigl, P. Grössing, *et al.*, "Tunable non-integer high-harmonic generation in a topological insulator," Nature **593**, 385–390 (2021).

29. P. J. van Essen, Z. Nie, B. de Keijzer, *et al.*, "Toward complete all-optical intensity modulation of high-harmonic generation from solids," ACS Photonics **11**, 1832–1843 (2024).

30. S. D. R. Abbing, R. Kolkowski, Z.-Y. Zhang, *et al.*, "Extreme-ultraviolet shaping and imaging by high-harmonic generation from nanostructured silica," Phys. Rev. Lett. **128**, 223902 (2022).

31. M. Sivis, M. Taucer, G. Vampa, *et al.*, "Tailored semiconductors for high-harmonic optoelectronics," Science **357**, 303–306 (2017).

32. P. Peterka, A. O. Slobodeniuk, T. Novotný, *et al.*, "High harmonic generation in monolayer MoS2 controlled by resonant and near-resonant pulses on ultrashort time scales," APL Photonics **8**, 086103 (2023).

33. K. Murzyn, L. Guery, Z. Nie, *et al.*, "Point-spread function reduction through high-harmonic generation deactivation," in *The European Conference on Lasers and Electro-Optics* (Optica, 2023), paper cf_2_3.

34. Y. Cheng, H. Hong, H. Zhao, *et al.*, "Ultrafast optical modulation of harmonic generation in two-dimensional materials," Nano Lett. **20**, 8053–8058 (2020).

35. K. Nagai, K. Uchida, S. Kusaba, *et al.*, "Effect of incoherent electron-hole pairs on high harmonic generation in an atomically thin semiconductor," Phys. Rev. Res. **5**, 043130 (2023).

36. S. Xu, H. Zhang, J. Yu, *et al.*, "Ultrafast modulation of a high harmonic generation in a bulk ZnO single crystal," Opt. Express **30**, 41350 (2022).

37. D. Shafir, H. Soifer, B. D. Bruner, *et al.*, "Resolving the time when an electron exits a tunnelling barrier," Nature **485**, 343–346 (2012).

38. S. R. Abbing, F. Campi, F. Sajjadian, *et al.*, "Divergence control of high-harmonic generation," Phys. Rev. Appl. **13**, 054029 (2020).

39. S. D. R. Abbing, F. Campi, A. Zeltsi, *et al.*, "Divergence and efficiency optimization in polarization-controlled two-color high-harmonic generation," Sci. Rep. **11**, 24253 (2021).

40. S. Heo, E. Cho, H.-I. Lee, *et al.*, "Band gap and defect states of MgO thin films investigated using reflection electron energy loss spectroscopy," AIP Adv. **5**, 077167 (2015).

41. H. Haug and S. W. Koch, *Quantum Theory of the Optical and Electronic Properties of Semiconductors* (World Scientific, 2009).

42. D. Golde, T. Meier, and S. W. Koch, "Microscopic analysis of extreme nonlinear optics in semiconductor nanostructures," J. Opt. Soc. Am. B **23**, 2559–2565 (2006).

43. K. J. Burns, G. M. Vasil, J. S. Oishi, *et al.*, "Dedalus: a flexible framework for numerical simulations with spectral methods," Phys. Rev. Res. **2**, 023068 (2020).

44. O. Schubert, M. Hohenleutner, F. Langer, *et al.*, "Sub-cycle control of terahertz high-harmonic generation by dynamical Bloch oscillations," Nat. Photonics **8**, 119–123 (2014).

45. S. D. C. R. Abbing, F. Campi, B. de Keijzer, *et al.*, "Efficient extreme-ultraviolet high-order wave mixing from laser-dressed silica," arXiv (2022).

46. P. Juergens, S. D. C. R. Abbing, M. Mero, *et al.*, "Linking high-harmonic generation and strong-field ionization in bulk crystals," ACS Photonics **11**, 247–256 (2024).

47. L. Yue and M. B. Gaarde, "Introduction to theory of high-harmonic generation in solids: tutorial," J. Opt. Soc. Am. B **39**, 535–555 (2022).

48. T. Meier, G. Von Plessen, P. Thomas, *et al.*, "Coherent electric-field effects in semiconductors," Phys. Rev. Lett. **73**, 902–905 (1994).

49. A. M. Fox, D. A. B. Miller, J. E. Cunningham, *et al.*, "Suppression of the observation of stark ladders in optical measurements on superlattices by excitonic effects," Phys. Rev. B **46**, 15365–15376 (1992).

50. P. Becker, H. Fragnito, C. B. Cruz, *et al.*, "Femtosecond photon echoes from band-to-band transitions in GaAs," Phys. Rev. Lett. **61**, 1647 (1988).

51. G. Moody, C. K. Dass, K. Hao, *et al.*, "Intrinsic homogeneous linewidth and broadening mechanisms of excitons in monolayer transition metal dichalcogenides," Nat. Commun. **6**, 8315 (2015).

52. S. T. Cundiff, "Effects of correlation between inhomogeneously broadened transitions on quantum beats in transient four-wave mixing," Phys. Rev. A **49**, 3114–3118 (1994).

53. C. Heide, T. Eckstein, T. Boolakee, *et al.*, "Electronic coherence and coherent dephasing in the optical control of electrons in graphene," Nano Lett. **21**, 9403–9409 (2021).

54. S. Ogawa, H. Nagano, H. Petek, *et al.*, "Optical dephasing in Cu(111) measured by interferometric two-photon time-resolved photoemission," Phys. Rev. Lett. **78**, 1339–1342 (1997).

55. B. R. Bennett, R. A. Soref, and J. A. Del Alamo, "Carrier-induced change in refractive index of InP, GaAs and InGaAsP," IEEE J. Quantum Electron. **26**, 113–122 (1990).

56. G. Vampa, C. McDonald, G. Orlando, *et al.*, "Theoretical analysis of high-harmonic generation in solids," Phys. Rev. Lett. **113**, 073901 (2014).

57. I. Floss, C. Lemell, K. Yabana, *et al.*, "Incorporating decoherence into solid-state time-dependent density functional theory," Phys. Rev. B **99**, 224301 (2019).

58. I. Floss, C. Lemell, G. Wachter, *et al.*, "Ab initio multiscale simulation of high-order harmonic generation in solids," Phys. Rev. A **97**, 011401 (2018).

59. G. Wang and T.-Y. Du, "Quantum decoherence in high-order harmonic generation from solids," Phys. Rev. A **103**, 063109 (2021).

60. G. Vampa and T. Brabec, "Merge of high harmonic generation from gases and solids and its implications for attosecond science," J. Phys. B **50**, 083001 (2017).

61. U. Huttner, K. Schuh, J. V. Moloney, *et al.*, "Similarities and differences between high-harmonic generation in atoms and solids," J. Opt. Soc. Am. B **33**, C22–C29 (2016).

62. S. Carlström, J. Preclíková, E. Lorek, *et al.*, "Spatially and spectrally resolved quantum path interference with chirped driving pulses," New J. Phys. **18**, 123032 (2016).